ELSEVIER

Advances in Water Resources 24 (2001) 11–27

Advances in Water Resources

www.elsevier.com/locate/advwatres

Three-dimensional wind-induced baroclinic circulation in rectangular basins

Yongqi Wang [a,*], Kolumban Hutter [a], Erich Bäuerle [b]

[a] *Institute of Mechanics, Darmstadt University of Technology, Hochschulstr. 1, D-64289 Darmstadt, Germany*
[b] *Limnological Institute, University of Constance, D-78457 Constance, Germany*

Received 29 July 1999; received in revised form 14 June 2000; accepted 15 June 2000

Dedicated to Professor K. Wilmanski on occasion of his 60th birthday

Abstract

We present results of various circulation scenarios for the wind-induced currents in two vertically stratified rectangular basins of constant depth with different sizes; these are obtained with the aid of a semi-spectral semi-implicit finite difference code developed in Haidvogel DB, Wilkin JL, Young R. J. Comput. Phys. 94 (1991) 151–185 and Wang Y, Hutter K. J. Comput. Phys. 139 (1998) 209–241. Our focus is to see whether the code allows reproduction of the many well-known processes exhibited in stratified waters of a lake basin on the rotating Earth. Often, the internal dynamics exhibits Kelvin- and Poincaré-type oscillations, whose periods depend upon the stratification and the geometry of the basin and which persist for a long time, the attenuation being the result of the turbulent dissipation mechanisms. It is shown that the numerical dissipation of our code can be sufficiently restricted that such wave dynamics obtained with it is realistically persistent for typical time scales of physical limnology. Direct responses to wind forcing and the oscillating behaviour after wind secession are studied and numerical results are illustrated for longitudinal and transverse winds, respectively. By solving the eigenvalue problem of the linearized shallow water equations of two-layered closed rectangular basins, the interpretation of the oscillations as Kelvin- and Poincaré-type waves is corroborated.

Keywords: Lake circulation; Limnology; Kelvin- and Poincaré-type oscillations

1. Introduction

The stratification in lakes is almost exclusively established by the heat input due to solar radiation. During the summer season, in temperate climate zones, a stratification given at one particular instant generally persists for a time span that is long in comparison to the time scales of the dynamic circulation which is established by the wind shear traction applied at the water surface. Only during short-lived episodes, when the shearing in the surface layer is very large (i.e., typically during strong storms), Kelvin–Helmholtz instabilities can form and generate internal bores that destroy the stratification or may erode the thermocline. During the short periods in-between the change of the stratification caused by the dynamic circulation is relatively small. Thus, a stable underlying stratification with no motion may be assumed as an initial condition from which the temperature and velocity field may develop without forming internal instabilities.

The underlying thermo-mechanical processes can mathematically be described by the shallow water equations in the Boussinesq approximation: in these equations the vertical momentum balance reduces to the force balance between pressure gradient and gravity (buoyancy) force, and density variations are only accounted for in the buoyancy term. The equations describe both, barotropic and baroclinic processes. The former are those that develop when density variations do not exist and, in temperate zones, arise in late autumn and during winter. They also exist in a truly stratified lake or ocean basin, but are then overshadowed by the baroclinic processes that are typical for the summer seasons when the underlying stratification is strong. We studied barotropic processes for ideal geometries and Lake Constance in [13]. Here we focus

* Corresponding author. Tel.: +49-6151-163196; fax: +49-6151-164120.

E-mail addresses: wang@mechanik.tu-darmstadt.de (Y. Wang), hutter@mechanik.tu-darmstadt.de (K. Hutter), Erich.Baeuerle@uni-konstanz.de (E. Bäuerle).

0309-1708/01/$ - see front matter
PII: S0309-1708(00)00034-8

upon baroclinic processes for ideal basins of rectangular geometry in order to eliminate the complicated effects of topography and irregular shore of a real lake from the baroclinic processes, reserving a detailed study for stratified Lake Constance to a further article [14].

The highly non-linear initial boundary value problem that describes wind induced circulation dynamics in enclosed basins will not be described in this paper; the reader is referred to [12]. Neither shall we describe in detail the semi-spectral primitive equation model (SPEM) with the aid of which the shallow water equations in the Boussinesq approximation are numerically solved for given external atmospheric driving. To that end the reader is directed to [12]. Here our aim is the presentation of explicit solutions to given stratification and wind stress scenarios. The reasons for our detailed investigation are as follows: classical finite difference and (less frequent) finite element implementations of the hydrodynamic equations in the shallow water and Boussinesq approximation with a Cartesian coordinate system are generally fraught with numerical diffusion that overshadows the physical diffusion of momentum and energy in magnitude. The probable reasons lie in the use of conditionally stable (explicit) integration techniques and in the low order accuracy of the discretization techniques. For usual spatial and temporal time steps (that obey the Courant–Friedrichs–Levy criterion) unduly large momentum and energy diffusivities are needed to make integrations possible. As a result, time dependent processes that are persistently created by the time-varying winds die out relatively quickly. In extreme cases, e.g., when an oscillating process should develop from a wind signal, the computed motion dies out before it even has had a chance to fully develop.

Because of the small size of lakes in comparison to the ocean, their boundaries transform the time dependent (oscillating) driving mechanisms into a response of current and temperature distributions which manifest themselves both in *quantized* components, characteristic of the geometry of the enclosed basins and the stratification plus a direct signal. The quantized component is reminiscent of the Kelvin and Poincaré wave dynamics and, during summer, often persists for days and weeks as conspicuous signals of water displacement in the metalimnion. Naturally, computational codes ought to reproduce this oscillatory motion, which explains why three-dimensional codes must adequately account for as little numerical diffusion as possible.

We believe that the version of SPEM with semi-implicit numerical integration as sketched below is particularly suitable to cope with such conditions, since numerical diffusion can be kept sufficiently low in order not to overshadow its physical counterpart. In Section 2 we briefly outline how the model works. In Section 3 various scenarios of wind-driven baroclinic processes in a rectangular basin with constant depth are studied and the predicted Kelvin- and Poincaré-type oscillations can be displayed in the results. In Section 4 by solving the eigenvalue problem of the linearized shallow water equations of a two-layered closed rectangular basin, the interpretation of the oscillations as Kelvin- and Poincaré-type waves can be ascertained. To study the influence of basin dimension on the baroclinic processes, the same computations as in Sections 3 and 4 are performed in Section 5 for a smaller rectangular basin. We conclude with a summary and some remarks in Section 6.

2. SPEM with curvilinear orthogonal coordinates

We briefly describe here the numerical model as constructed by Haidvogel et al. [5] and changed by us to allow large-time-temporal integration [12].

2.1. Basic equations

The basic hydrodynamic equations consist of the balance equations of mass, momentum and energy as well as a thermal equation of state; here the following simplifying assumptions are invoked:

- *Boussinesq assumption*, i.e., density variations are only accounted for in the buoyancy term, and balance of mass reduces to the continuity equation ($\operatorname{div} \boldsymbol{v} = 0$).
- *Shallow water assumption*, i.e., the vertical momentum balance reduces to the hydrostatic equation balancing the vertical pressure gradient with the buoyancy force, and the effects of the eccentric rotation (second Coriolis parameter) are ignored.
- *Rigid lid assumption*, i.e., in the vertically integrated mass balance the influence of the motion of the free surface is ignored. This amounts to assuming the volume transport to be solenoidal and derivable from a stream function that can be determined independently of the baroclinic response.

Thus, under these assumptions the field equations read:

$$\frac{\partial u}{\partial x} + \frac{\partial v}{\partial y} + \frac{\partial w}{\partial z} = 0,$$

$$\frac{\partial u}{\partial t} + \boldsymbol{v} \cdot \operatorname{grad} u - fv = -\frac{\partial \phi}{\partial x} + \frac{\partial}{\partial x}\left(\nu_{\mathrm{H}} \frac{\partial u}{\partial x}\right) + \frac{\partial}{\partial y}\left(\nu_{\mathrm{H}} \frac{\partial u}{\partial y}\right) + \frac{\partial}{\partial z}\left(\nu_{\mathrm{V}} \frac{\partial u}{\partial z}\right),$$

$$\frac{\partial v}{\partial t} + \boldsymbol{v} \cdot \operatorname{grad} v + fu = -\frac{\partial \phi}{\partial y} + \frac{\partial}{\partial x}\left(\nu_{\mathrm{H}} \frac{\partial v}{\partial x}\right) + \frac{\partial}{\partial y}\left(\nu_{\mathrm{H}} \frac{\partial v}{\partial y}\right) + \frac{\partial}{\partial z}\left(\nu_{\mathrm{V}} \frac{\partial v}{\partial z}\right),$$

$$
\begin{aligned}
0 &= -\frac{\partial \phi}{\partial z} - \frac{\rho g}{\rho_0}, \\
&\frac{\partial T}{\partial t} + \boldsymbol{v} \cdot \operatorname{grad} T \\
&\quad = \frac{\partial}{\partial x}\left(D_{\mathrm{H}}^{T} \frac{\partial T}{\partial x}\right) + \frac{\partial}{\partial y}\left(D_{\mathrm{H}}^{T} \frac{\partial T}{\partial y}\right) + \frac{\partial}{\partial z}\left(D_{\mathrm{V}}^{T} \frac{\partial T}{\partial z}\right), \\
&\frac{\rho - \rho_0}{\rho_0} = -6.8 \times 10^{-6} \times (T - T_0)^2 \quad (T \text{ in } ^\circ\mathrm{C}).
\end{aligned}
\tag{1}
$$

Here a Cartesian coordinate system (x, y, z) has been used; (x, y) are horizontal, and z is vertically upwards, against the direction of gravity; $\boldsymbol{v} = (u, v, w), f, \rho, \rho_0, \phi, g, T$ are, respectively, the velocity vector, Coriolis parameter, density, reference density ($\rho_0 = 1000$ kg m^{-3} at temperature $T_0 = 4^\circ$C), dynamic pressure ($\phi = p/\rho_0$, p is pressure), gravity force ($g = 9.8$ m s^{-2}), temperature. Furthermore, $\nu_{\mathrm{H}}, \nu_{\mathrm{V}}$ are horizontal and vertical momentum, D_{H}^{T}, D_{V}^{T}, horizontal and vertical heat diffusivities. A derivation of these equations from a proper scaling analysis is, e.g., given by Hutter [6]. We note that dispersion in integrated layer models is due to the inclusion of the acceleration terms in the vertical momentum balance and necessarily stabilizes those models both physically and computationally. This is one reason why hydrostatic models generally require a large amount of numerical diffusion and is no different in SPEM.

2.2. Original version of SPEM

Haidvogel et al. [5] developed a SPEM from the hydrodynamic equations (1). In SPEM, smoothness in the representation of the discretization is the principle to minimize the necessary numerical diffusion; hydrostaticity is maintained. To this end the σ-transformation in the vertical direction, mapping irregular lake topography into constant depth (in the σ-coordinate), and the Schwarz–Chrystoffel transformation in the horizontal, mapping the irregular lake shoreline onto a rectangle, are implemented, viz.,

$$
\xi = \xi(x, y), \quad \eta = \eta(x, y), \quad \sigma = 1 + 2\frac{z}{h(x, y)}, \tag{2}
$$

where $h(x, y)$ is the lake depth. The computational domain becomes now a cube in (ξ, η, σ)-space. This transformation avoids step-like discontinuous approximations of the lake boundary in FD-approximations which could also be achieved by using FE-approximations. Of course, for a rectangular basin such a transformation is unnecessary. In SPEM, the vertical σ-dependence of the model variables is represented as an expansion in a finite polynomial basis set $\{T_k(\sigma)\}$, that is,

$$
b(\xi, \eta, \sigma, t) = \sum_{k=0}^{N} T_k(\sigma) \hat{b}_k(\xi, \eta, t), \tag{3}
$$

where b is any unknown field variable, $\{T_k(\sigma)\}$ is a set of orthogonal polynomials defined in $[-1, 1]$, the only restriction placed on their form is that

$$
\int_{-1}^{1} T_k(\sigma)\, \mathrm{d}\sigma = 2\delta_{k0},
$$

where δ_{k0} is the Kronecker delta – i.e., only the lowest order polynomial ($k = 0$) has a non-zero vertical integral. This isolates the depth averaged barotropic component of the field. $\{T_k(\sigma)\}$ are chosen to be modified Chebyshev polynomials, and the expansion guarantees a very smooth representation of the variables in the σ-direction if only N is sufficiently large. In the horizontal, i.e., the ξ, η-directions, finite difference representations with an Arakawa C-grid are used.

SPEM in its original version employs an explicit scheme for temporal integration and thus is numerically only conditionally stable, i.e., the allowable time step is restricted by the horizontal resolution and the number N of polynomials taken into account in (3). This conditional stability also dictates which numerical values the horizontal and vertical diffusivities of momentum and energy can take. Because of the smoothness precautions taken in (2) and (3) these values are of the order of what would be physically suggested (or somewhat larger) but the temporal steps of integration are still prohibitively small for many problems.

2.3. Implementation of semi-implicit integration in time

A fully implicit integration in time is equally prohibitive because of the large non-linear systems of equations that emerge; so we considered alternate direction implicit (ADI) procedures. Accordingly, the integration step from time level n to $n + 1$ is subdivided as follows:

1. $t^n \to t^{n+1/3}$, implicit in ξ-direction, explicit in η- and σ-directions,
2. $t^{n+1/3} \to t^{n+2/3}$, implicit in η-direction, explicit in ξ- and σ-directions,
3. $t^{n+2/3} \to t^{n+1}$, implicit in σ-direction, explicit in ξ- and η-directions.

It turned out that for usual lakes tripling the time step Δt according to this procedure is less effective than to employ a semi-implicit integration in the σ-direction alone with the full time step Δt. Furthermore, computations for barotropic wind induced processes in Lake Constance showed that time steps could be 200–400 times larger than with the explicit integration of the original SPEM while the computational time could be reduced by a factor of 60. For baroclinic processes the gain is much less but still a factor of approximately 20, or more for time steps and a factor of 6 for the computational time, respectively.

A detailed analysis of this, including a study of selection of the optimal horizontal and vertical diffusivities is given by Wang and Hutter [12].

3. Wind-induced baroclinic response in a rectangular basin

3.1. Parameter and scenario setting

This model is driven by prescribing at each nodal point on the free surface of the discretized domain time series of the shear-traction vector (its ξ- and η-components) and the surface temperature or surface heat low. In principle, therefore, arbitrary spatial distributions of the wind forcing can be prescribed if so desired, however, we will here restrict attention to relatively simple scenarios: uniformly distributed wind in a preferred direction and Heaviside-type in time, e.g., uniform in space and constant in time wind only lasting the first two days. A wind speed of $V_{\text{wind}} = 5$ m s^{-1}, 10 m above the water surface, is used, corresponding to a wind stress of 0.055 N m^{-2} at the water surface. Similarly, basal shear tractions obey a viscous sliding law. As for other boundary conditions, the rigid lid assumption is applied at the free surface and the low is tangential to the bed. Furthermore, it will be assumed that no heat lows across the free or basal surfaces: $\mathrm{d}T/\mathrm{d}\boldsymbol{n} = \boldsymbol{0}$, where $\boldsymbol{n}$ is the unit normal vector of the boundary surface.

We shall now apply our model to a rectangular basin with constant depth and subject it to an initial stratification as prescribed below. Length, width and depth of the rectangle are 65 km, 17 km and 100 m, respectively. The mesh size will be $\Delta x = \Delta y = 1$ km, whereas in the vertical 30 Chebyshev-polynomials will be employed.

The stratification varies seasonally following that the solar radiation heats the upper most layers of the lake, and turbulence diffuses this heat to greater depths. By late summer these processes will have established a distinct stratification, that essentially divides the water mass into a warm upper layer (called epilimnion), a cold deep layer (hypolimnion) which are separated by a transition zone (metalimnion), in which the epilimnion temperatures above it are transferred to the hypolimnion temperatures below it. Vertical temperature gradients in this layer are larger than in the epi- and hypolimnion with a maximum at the so-called thermocline. A vertical temperature profile, typical of a late summer situation for Alpine lakes (see, e.g., [2,7]), is

$$T(t=0) = \begin{cases} 17 - 2\exp(-(z+20)/5), & z \geqslant -20 \text{ m} \\ 5 + 10\exp((z+20)/20), & z < -20 \text{ m} \end{cases} [^\circ\text{C}], \tag{4}$$

it will be chosen as the initial temperature profile from which also the initial density distribution can be computed according to the thermal equation of state, the sixth equation of (1). For computational and physical purposes this representation is sufficiently accurate. We shall later present results for the internal eigen-oscillations also on the basis that the continuous stratification is replaced by a two-layer model, consisting of an epilimnion with constant density and a hypolimnion equally with constant but larger density separated at the thermocline by a sharp material interface.

The computations of the baroclinic currents is performed for the following choices of diffusivities $v_{\text{H}}, v_{\text{V}}$ of momentum, and $D^T_{\text{H}}, D^T_{\text{V}}$ of heat, respectively:

$$v_{\text{V}} = \begin{cases} 0.016, & z > -20 \text{ m}, \\ 0.0016, & -20 \text{ m} \geqslant z \geqslant -40 \text{ m}, \\ 0.008, & z < -40 \text{ m} \end{cases} \quad [\text{m}^2 \text{ s}^{-1}],$$

$$v_{\text{H}} = 1.0 \text{ m}^2 \text{ s}^{-1},$$

$$D^T_{\text{V}} = \begin{cases} 0.0002, & z > -20 \text{ m}, \\ 0.00002, & -20 \text{ m} \geqslant z \geqslant -40 \text{ m}, \\ 0.00004, & z < -40 \text{ m} \end{cases} \quad [\text{m}^2 \text{ s}^{-1}],$$

$$D^T_{\text{H}} = 1.0 \text{ m}^2 \text{ s}^{-1}, \tag{5}$$

in which the horizontal diffusivities are simply chosen as constants. For the non-constant vertical diffusivities, this choice accounts for the fact that the Austausch coefficients are considerably smaller in the metalimnion region than in the epilimnion above and the hypolimnion below. This is so because the thermocline prevents diffusion through this 'interface'. The diffusivities in the hypolimnion are also smaller than in the epilimnion because of its smaller ambient turbulence. Compared with realistic measured values they are basically in the range that is thought to be physically acceptable, even though they are still somewhat larger than measured values [6,8,11]. Computations with even smaller diffusivities can also be performed if for numerical stable considerations higher vertical resolution (larger number of Chebyshev polynomials) is used, of course, therefore longer computational time is needed.

In the following two subsections the simulated results are displayed and discussed for winds in the longitudinal and transverse direction, respectively, lasting only the first two days.

3.2. Uniform wind in the longitudinal direction

In this subsection we consider the response of the rectangular basin to an impulsively applied constant wind force in the longitudinal direction from west with a duration of two days. The model is started at rest and integrated over a period of 12 days.

Fig. 1 shows time series of the vertical velocity component w in 30 and 60 m depth, respectively, at the four

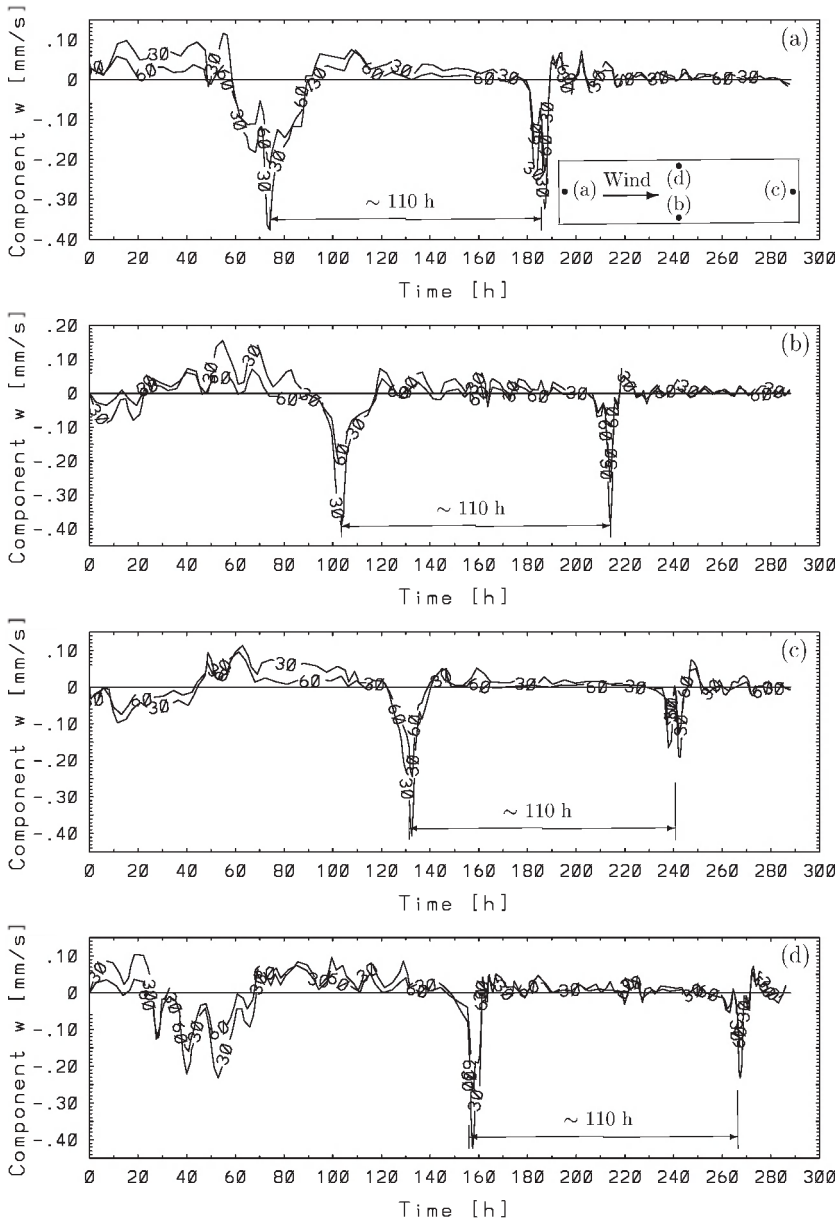

Fig. 1. Time series of the vertical velocity component w at the four near-shore midpoints, counterclockwise around the basin (western (a), southern (b), eastern (c) and northern shore (d) indicated in the inset) at 30 and 60 m depths in the stratified rectangular basin of constant depth subject to constant wind from west (in the long direction) lasting two days. The labels correspond to the depths (30 and 60 m).

near-shore midpoints as sketched in panel (a) of Fig. 1. Immediately after the westerly wind set up, the motion starts with an upwelling at the western end and a downwelling at the eastern end due to the direct effect of wind stress at the surface. In the northern (southern) mid boundary points there occurs initially an upwelling (downwelling). This behavior is, clearly, due to the Coriolis force that causes a velocity drift to the right and therefore is responsible for the initial downwelling (upwelling) at the southern (northern) shore. The motion is characterized by oscillation, of which two conspicuous components can be clearly identified. The longer periodic oscillation, barely visible in the overall behaviour but conspicuously indicated by the strong downstroke signals, can be identified as an internal Kelvin-type wave, the shorter periodic one as a Poincaré-type wave. We will in the next section provide convincing details for this interpretation. In Fig. 1(a) for the western shore point the downstroke after the wind secession (48 h) is conspicuously seen at ~73 h. If we follow this downwelling signal around the lake, then it is seen in panels (a)–(d) of Fig. 1 at ~74, 104, 133, 158 h. As the next downwelling signal it emerges again at ~186, 213, 240, 264 h, respectively, the four points are encountered counterclockwise around the basin, with a travel time of approximately 105–110 h around the basin. Fig. 1 also

discloses very clearly the short periodic oscillations that are superimposed on the long term trend in the signals. This oscillating signal may be interpreted as a standing Poincaré-type wave. These waves persist for a very long time, for more than 10 days, as one can also observe in real lakes.

The Kelvin-type oscillations can be seen even more clearly in the isotherm-depth time series at the same four near-shore midpoints displayed in Fig. 2. This figure clearly shows that the metalimnion experiences a strong downward motion whenever the downwelling strokes indicated in Fig. 1 pass the respective position emphasized by the arrows in Fig. 2. After the rapid downward motion the isotherms rise again, much more slowly though, until the second rapid downward motion is initiated by the second passage of the downwelling signal. If instead of isotherm-depth-time series temperature-time series at a certain depth are drawn, the graphs of Fig. 3 are obtained. These graphs are better suited to show the epilimnetic and hypolimnetic behaviour, but they also disclose the conspicuous motion in the metalimnion. This motion circulates counterclockwise around the basin with a period of $T_k \sim 110$ h. In the epilimnion (above ~15 m depth) and in the hypolimnion (below ~45 m depth) the temperature change is relatively small. It is mainly caused by the vertical motion of the thermocline (metalimnion); the changes associated with direct thermal diffusion are relatively small. Contrary to this Kelvin-type behaviour, the Poincaré-type oscillation cannot be identified in the isotherm-depth- and temperature-time series of Figs. 2 and 3. Neither can they be discerned in corresponding isotherm depth or temperature-time series at mid-lake positions. This is so because of the very small vertical velocities occurring at mid-lake positions; except for a small temperature drop at the beginning which is due to turbulent mixing these temperature results give no conclusive inferences (not shown here for brevity).

Fig. 4 shows the longshore velocity at the mid-points of the western (a), southern (b), eastern (c) and northern shores (d) as functions of time at various vertical locations. As expected, the Kelvin-type wave may be clearly identified. The vertical structure of the current field exhibits first baroclinic mode behaviour in that the horizontal velocity oscillates above the metalimnion with the opposite phase from that below the metalimnion; this is very similar to the result of a two-layer model. In the metalimnion the amplitudes of the oscillation of the horizontal velocity is relatively small. Furthermore, the times of vanishing horizontal motion separate a 110 h interval, the suspected Kelvin wave period; these times occur simultaneously at the midpoints of western and eastern shores and a quarter period (28 h) later at southern and northern shore, as expected. In other words, this position of vanishing horizontal motion travels counterclockwise around the basin.

In Fig. 5 the time series of the horizontal velocity components u (a) and v (b) in the center of the basin at 0 m and 60 m depths are displayed. It is known that

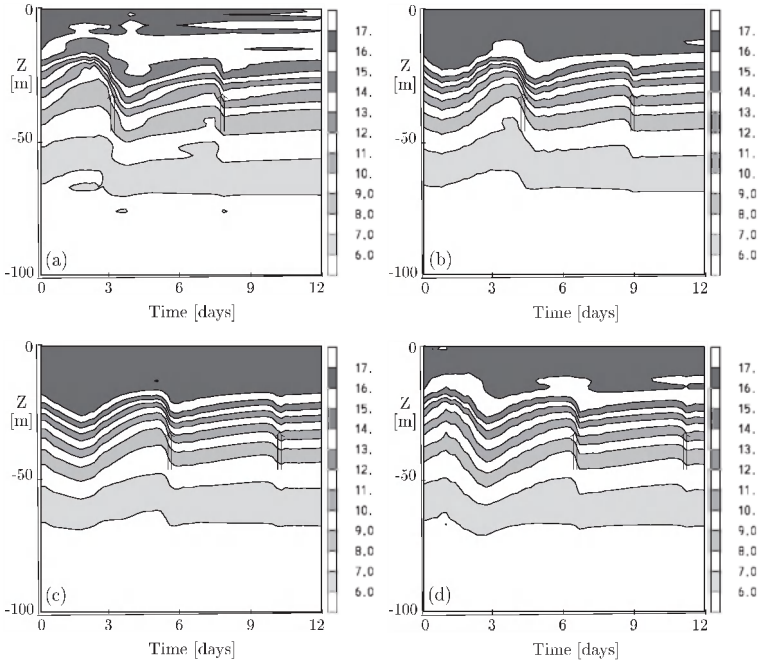

Fig. 2. Isotherm-depth time series at the four near-shore midpoints, counterclockwise around the basin (western (a), southern (b), eastern (c) and northern shore (d)) in the stratified rectangular basin of constant depth subject to a constant wind from west (in the longitudinal direction) lasting two days. The labels correspond to the temperatures in °C.

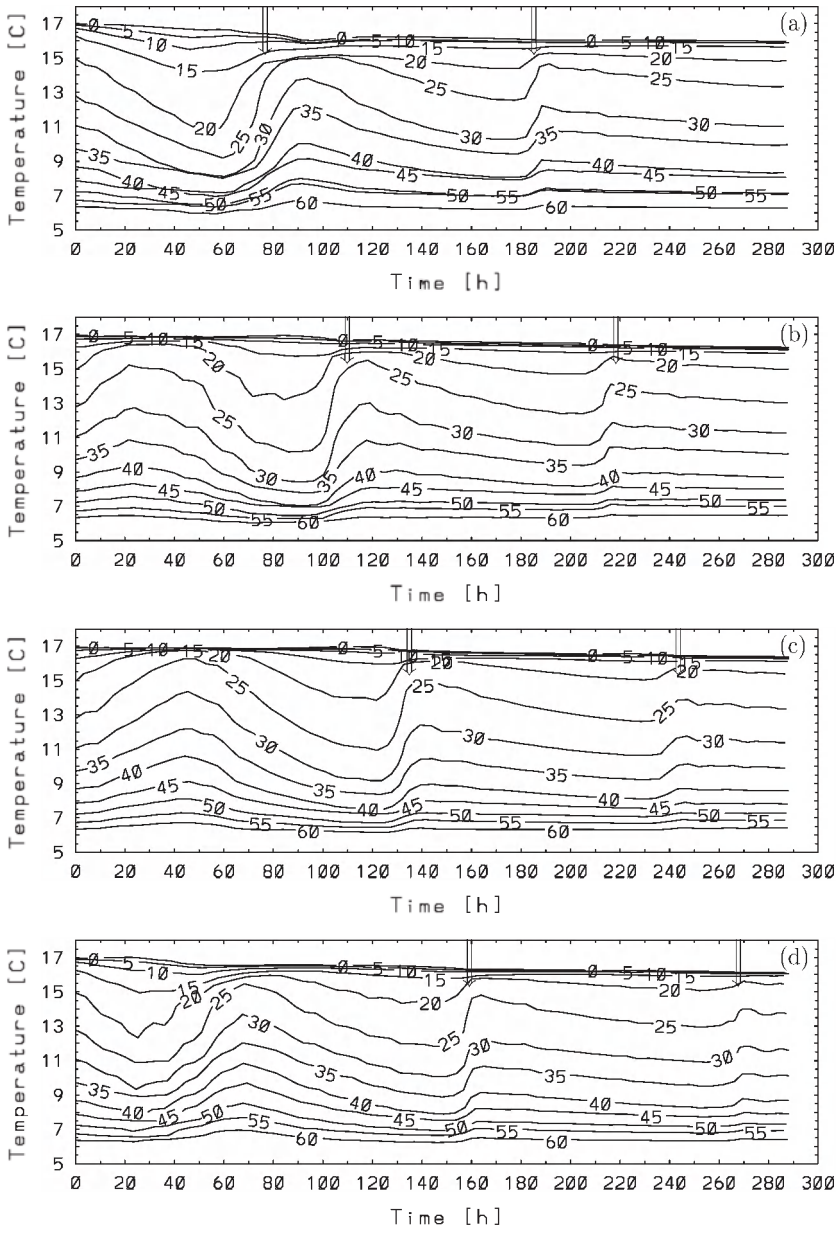

Fig. 3. Time series of the temperature at the four near-shore midpoints, counterclockwise around the basin (western (a), southern (b), eastern (c) and northern shore (d)) at various depths in the stratified rectangular basin of constant depth subject to a constant wind from west (in the longitudinal direction) lasting two days. The labels correspond to the depths in meters.

rotational effects on gravitational waves (e.g., Kelvin and Poincaré waves) can be detected in basins which are wide as compared, or at least comparable to the Rossby radius $R = c_{\text{int}}/f$, where c_{int} is the phase speed of internal gravitational waves. The Rossby radius measures a critical length scale over which rotation is important for the dynamics of the motion. For baroclinic waves R is just a few kilometers. We will see in the next section that the phase speed of the internal baroclinic waves for the stratification (4) is nearly $c_{\text{int}} \simeq 0.39\ \text{ms}^{-1}$, which corresponds to a Rossby radius of $R \simeq 3.7$ km for a Coriolis parameter $f = 1.07 \times 10^{-4}\ \text{s}^{-1}$. The amplitude of a Kelvin-type wave decays exponentially as one moves away from the boundary, the decay rate being given by the Rossby radius. Even though Kelvin-type waves decay with the distance from shore, this kind of oscillation can still be recognized in the middle of the lake if the lake width does not extend over more than three or four Rossby radii. This is the case here. Obviously, the amplitude of Kelvin-type waves in the center of the basin is much smaller than near-shore. As opposed to the temperature signal, for which an amphidromic point results at the centre of the rectangle, the remaining contributions of the shore-parallel currents which are equally oriented at opposite shores, are added together. For $R = 3.7$ and $B = 17$ km one would have the long

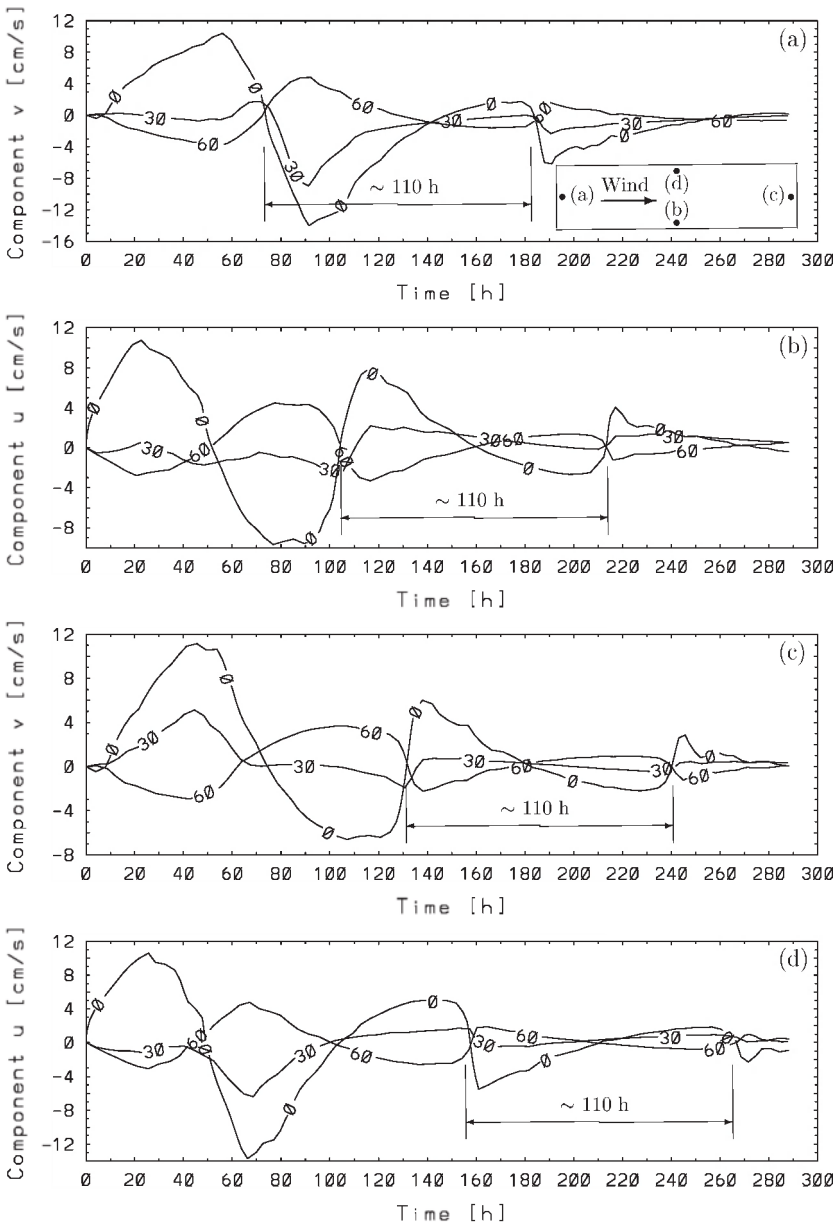

Fig. 4. Time series of the shore-parallel velocity component at the four near-shore midpoints, counterclockwise around the basin (western (a), southern (b), eastern (c) and northern shore (d) indicated in the inset) at various depths in the stratified rectangular basin of constant depth subject to a constant wind from west (in the longitudinal direction) lasting two days. The labels correspond to the depths in meters.

velocity component in the middle, if friction can be excluded,

$$u(y = B/2) = (u(y = 0) + u(y = B)) \exp\left(-\frac{B}{2R}\right)$$
$$= 2\overline{u}_{\text{shore}} \exp\left(-\frac{8.5}{3.7}\right) = 0.2\overline{u}_{\text{shore}},$$

which agrees well with the computational results (compare $u(z = 0)$ at the time $t = 90$ h in Figs. 4(a) and (c) ($\overline{u} = (14 + 6)/2$ cm s^{-1}) with $u(z = 0)$ at $t = 90$ h in Fig. 5, once the Poincaré contributions are subtracted. When the amplitude near the shore amounts approximately to 10–12 cm s^{-1}, it will be reduced to 2 cm s^{-1} in the middle of the lake.

Evidence of the second, transverse Poincaré-type waves, can be more clearly found in the middle of the lake, especially in the transverse component of the velocity. From the component of the velocity u, a superposition of Kelvin- and Poincaré-type waves can be identified, but in the transverse component v nearly only Poincaré-type waves exist with a period of approximately $T_p = 13.3$ h. One typical feature of Poincaré waves is that the horizontal projection of the velocity vector rotates clockwise (on the northern hemisphere). This behaviour can be inferred from the two panels in

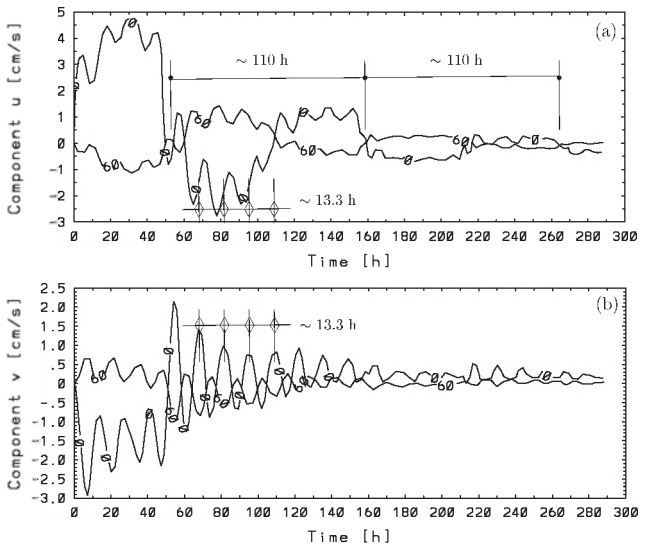

Fig. 5. Temporal evolution of the horizontal velocity components u (a) and v (b) for a midlake position in the stratified rectangular lake of constant depth subject to a constant wind from west (in the longitudinal direction) lasting two days. The labels correspond to the depths in meters. The diamond symbols mark times at which v reaches a maximum and u lies between a relative minimum and maximum. Two types of oscillations can be clearly seen with periods of approximately 13.3 and 110 h, respectively.

Fig. 5, where the diamond symbols mark times at which v reaches a maximum and u lies between a relative minimum and maximum. This is reminiscent of a 45° phase shift of the y-component behind the x-component, exactly what is expected by a Poincaré-type wave.

For a horizontally infinitely extended basin with a constant depth the vertical component of the velocity remains always zero under the action of a horizontal, spatially uniform wind-forcing. If the basin is horizontally bounded, the influence of the horizontal boundary propagates from the boundary toward the center of the basin. In a bounded domain at a given point away from the boundary of the basin the vertical component of the velocity vector is zero as long as no signal from an encounter with a horizontal boundary reaches this point. The perturbation induced by such an encounter propagates with the phase speed of the wave. Fig. 6 shows the distribution of the vertical component w of the velocity in the cross-section through the basin center for the first 6 h after the wind set-up. It can be clearly seen by comparison of the curves for various times that the perturbation propagates away from the boundary toward the lake center. Immediately after the onset of the wind from the West, due to the effect of the Coriolis force, the vertical motion in this mid-lake cross section commences with a downwelling (negative w) at the southern shore and an upwelling (positive w) near the northern shore. As time proceeds the regions of down- and upwelling become larger, as they move towards the mid-point of the lake. It takes nearly 6 h until the

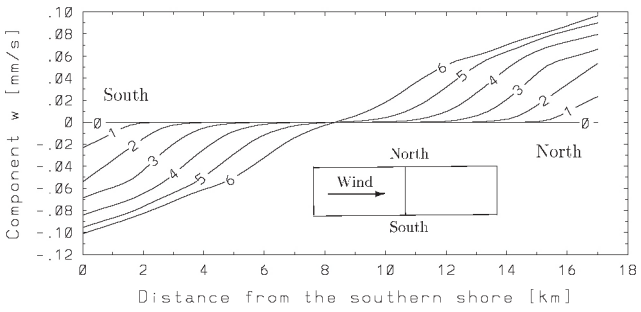

Fig. 6. Distribution of the vertical velocity component w at the cross-section through the midlake (indicated in the inset) at 30 m depth for the first 6 h after the wind set-up. The labels correspond to the time in hours.

perturbation reaches the center of the basin, 8.5 km from shore. This propagation speed amounts to approximately 0.4 m s^{-1}. We will see in Section 4 that this speed is almost exactly equal to the Kelvin-type phase speed of internal oscillations with stratification (4), obtained by solving an eigenvalue problem of the vertical velocity component. If we observe the vertical velocity component at the western and eastern ends for short times after the onset of the wind, a similar behaviour is observed.

As we have showed, for the chosen diffusivities (5), the Kelvin- and Poincaré-type waves could be easily identified. These waves persisted for a long time. If we repeat the same computation but using the ten times larger vertical diffusivities (which are obviously much larger than physically acceptable) than listed in (5), the oscillations can no longer be detected in the wind-deduced motion. In Fig. 7 the time series are displayed of the horizontal velocity components u and v computed with these larger diffusivities in the center of the basin at the free surface and 60 m depth, respectively. In this

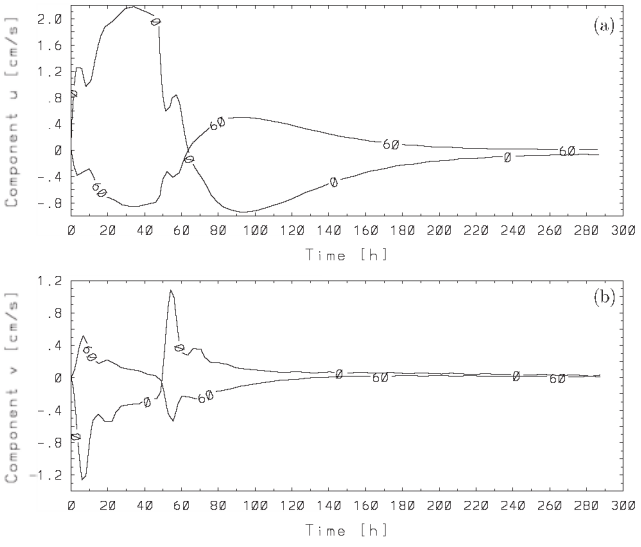

Fig. 7. Same as Fig. 5 but now computed with the 10 times larger vertical diffusivities than in Fig. 5.

case, transient Kelvin-type and Poincaré waves develop only within a short time after the wind set-up and secession while they are largely damped away before they are fully developed. After the wind secession the velocities die out very rapidly basically without any superimposed oscillations.

3.3. Uniform wind in the transverse direction

It is known that for wind-forcing in the transverse direction the Poincaré-type waves are more easily excited. We also performed computations for an uniform transverse wind (from South) lasting two days. Fig. 8 shows the longshore velocity components at the four mid-points of the shore around the basin. From these time series the superposition of the Poincaré-type oscillations on the long periodic Kelvin-type wave can be clearly identified. On the other hand, as we have seen in Fig. 4, for a wind in the longitudinal direction of the basin, this kind of transverse wave could not at all be identified from the horizontal velocity near the shore in that case. Strong Poincaré-type oscillations generated by a transverse wind can still be more easily identified in time series of the horizontal velocity components in the center of the basin (Fig. 9). Here no sign of a Kelvin-type response is discernable, quite contrary to

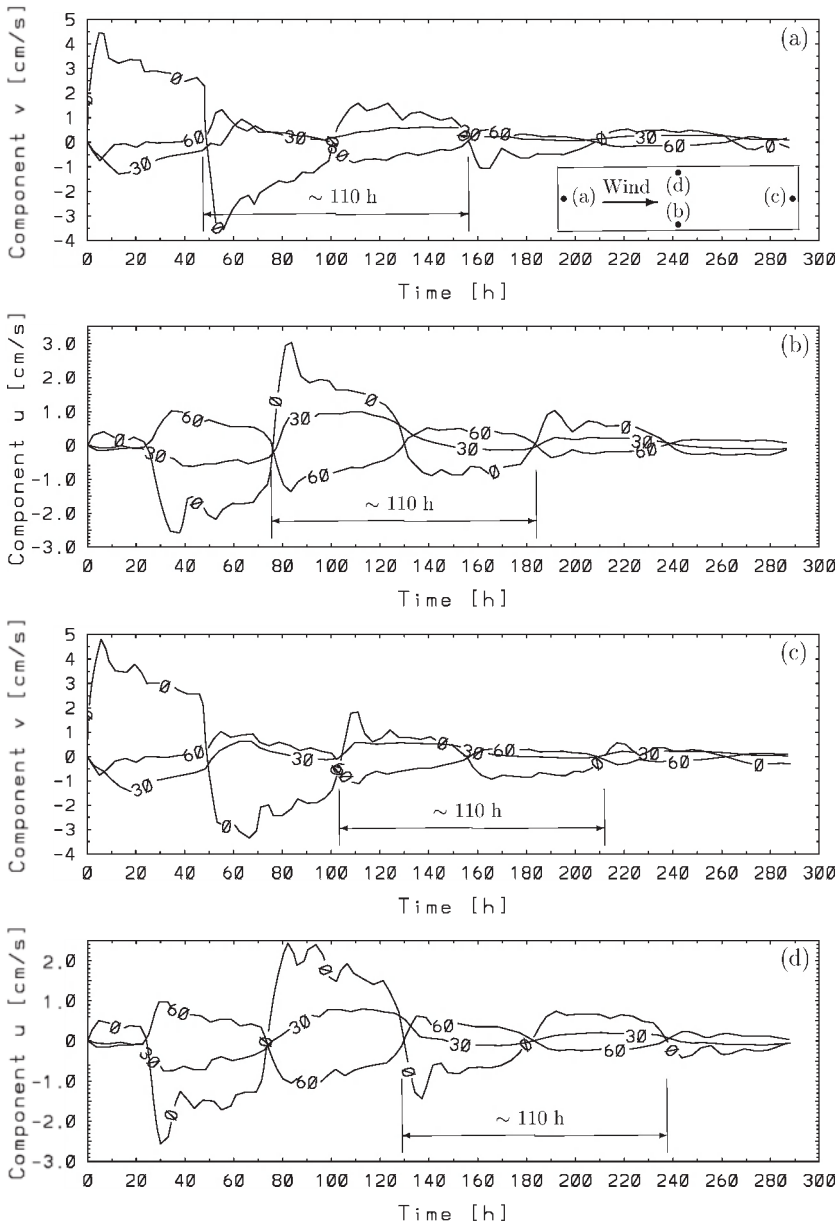

Fig. 8. Time series of the shore-parallel velocity component at the four near-shore midpoints, counterclockwise around the basin (western (a), southern (b), eastern (c) and northern shore (d) indicated in the inset) at various depths in the stratified rectangular basin of constant depth subject to constant wind from south (in the transverse direction) lasting two days. The labels correspond to the depths in meters.

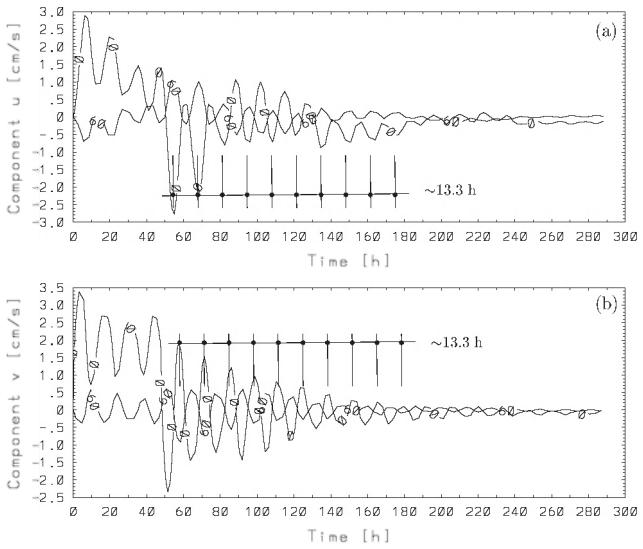

Fig. 9. Temporal evolution of the horizontal velocity components u (a) and v (b) for a midlake position in the stratified rectangular lake of constant depth subject to constant wind from south (in the transverse direction) lasting two days. The labels correspond to the depths in meters.

what was seen in panel (a) of Fig. 5 for a longshore wind.

4. Internal seiches: an eigenvalue problem of the two-layer model

To corroborate the interpretation of the oscillations emerging from the wind-induced motion, an eigenvalue problem is now solved. The ensuing analysis of free oscillations in this rectangular basin will be based upon a two-layer fluid system on the rotating Earth. We employ the shallow water equations of a two-layer fluid, ignore frictional effects and thus may suppose the layer velocity vectors to be independent of the depth coordinate. The depth integrated *linearized* momentum and conservation of mass equations then take the form (see, e.g., [8])

$$\begin{aligned}
&\frac{\partial \boldsymbol{V}_1}{\partial t} + f\boldsymbol{k}\times\boldsymbol{V}_1 + gh_1 \text{ grad } \zeta_1 = 0,\\
&\frac{\partial \zeta_1}{\partial t} + \text{div } \boldsymbol{V}_1 + \text{div } \boldsymbol{V}_2 = 0,\\
&\frac{\partial \boldsymbol{V}_2}{\partial t} + f\boldsymbol{k}\times\boldsymbol{V}_2 + g(1-\epsilon)h_1 \text{ grad } \zeta_1 + g\epsilon h_2 \text{ grad } \zeta_2 = 0,\\
&\frac{\partial \zeta_2}{\partial t} + \text{div } \boldsymbol{V}_2 = 0
\end{aligned} \tag{6}$$

with the boundary conditions for a closed water basin

$$\boldsymbol{V}_1\cdot\boldsymbol{n} = 0 \text{ and } \boldsymbol{V}_2\cdot\boldsymbol{n} = 0. \tag{7}$$

Here, f is the Coriolis parameter, $\boldsymbol{k}$ a unit vector in the z-direction and g the gravity constant. $\boldsymbol{V}_i$ $(i = 1, 2)$ are the horizontal components of the volume transport vector in the ith layer; ζ_i is the displacement of the free surface and interface, h_i the layer depth and $\epsilon = (\rho_2 - \rho_1)/\rho_2$, where ρ_i are the constant densities of the two layers, respectively. $\boldsymbol{n}$ is the unit normal vector along the boundary.

For constant depth basins, $h = h_1 + h_2 = \text{const.}$, the two-layer equations (6) and (7) can be decoupled into two one-layer models governing the free barotropic and baroclinic oscillations separately. In these new equations the horizontal motion is either unidirectional in the entire water column and then models the barotropic response, or back and forth in the epi- and hypolimnion with compensating mass transport and then models the baroclinic internal response. The equations for these latter free oscillations are:

$$\begin{aligned}
&\frac{\partial \boldsymbol{V}_{\text{int}}}{\partial t} + f\boldsymbol{k}\times\boldsymbol{V}_{\text{int}} + gh_{\text{int}} \text{ grad } \zeta_{\text{int}} = 0.\\
&\frac{\partial \zeta_{\text{int}}}{\partial t} + \text{div } \boldsymbol{V}_{\text{int}} = 0,\\
&\boldsymbol{V}_{\text{int}}\cdot\boldsymbol{n} = 0 \text{ along the boundary}
\end{aligned} \tag{8}$$

with

$$\begin{aligned}
&h_{\text{int}} = \epsilon\frac{h_1h_2}{h} + \text{O}(\epsilon^2), \quad \boldsymbol{V}_{\text{int}} = \boldsymbol{V}_1 - \frac{h_1}{h_2}\boldsymbol{V}_2 + \text{O}(\epsilon),\\
&\zeta_{\text{int}} = \zeta_1 - \frac{h}{h_2}\zeta_2 + \text{O}(\epsilon)
\end{aligned} \tag{9}$$

and

$$c_{\text{int}}^2 = gh_{\text{int}} = g\frac{\rho_2-\rho_1}{\rho_2}\frac{h_1h_2}{h_1+h_2}. \tag{10}$$

c_{int} is the phase speed of the internal gravity wave of the two-layer model and h_{int} the corresponding reduced depth. Using the harmonic ansatz

$$(\boldsymbol{V}_{\text{int}}(x,y,t), \zeta(x,y,t)) = (\boldsymbol{V}_{\text{int}}^*(x,y), \zeta^*(x,y))\text{e}^{\text{i}\omega t}, \tag{11}$$

with frequency ω and the amplitude $\boldsymbol{V}^*$ and ζ^* in Eq. (8) an eigenvalue problem emerges for the eigenvalue ω and the mode functions $\boldsymbol{V}^*$ and ζ^* which can be routinely determined [1].

For constant depth basins the same decomposition also exists for continuously stratified water bodies with the difference that now a countable spectrum of baroclinic modes exists of which the highest frequency corresponds to the above baroclinic solution of the two-layer model. Incorporating the rigid lid assumption one must solve in this case the problem [9]

$$N^2(z)\text{div grad } w + \left(\frac{\partial^2}{\partial t^2} + f^2\right)\frac{\partial^2 w}{\partial z^2} = 0$$

with

$$N^2(z) = -\frac{g}{\rho^*}\frac{\partial \rho}{\partial z}, \quad w = 0 \quad \text{at } z = 0,\ z = -h, \tag{12}$$

for the vertical component of the velocity field, w; ρ^* and $\rho(z)$ are a reference density and the vertical density profile and N is the so-called buoyancy frequency. With the separation solution $w(x,y,z,t) = Z_n(z)w_n(x,y,t)$ the Sturm–Liouville eigenvalue problem

$$\frac{\mathrm{d}^2 Z_n}{\mathrm{d}z^2} + \frac{N^2(z)}{gh_n}Z_n = 0, \quad Z_n = 0 \quad \text{at } z = 0 \quad \text{and } z = -h \tag{13}$$

emerges which possesses a countably infinite set of eigenvalues $c_n^2 = gh_n$ and associated eigenfunctions. The largest of these eigenvalues is identified with $c_{\text{int}}^2 = gh_{\text{int}}$ of the two-layer problem (8)–(11). With the temperature distribution (4) the solution of this vertical mode is $c_{\text{int}} = \sqrt{gh_{\text{int}}} = 0.391$ m s^{-1}, corresponding to a two-layer situation with $h_1 = 20$ m, $h_2 = 80$ m and $\epsilon = 9.741 \times 10^{-4}$. Using this value of c_{int} in Eqs. (8)–(11) allows evaluation of the *horizontal* structure of the corresponding oscillations. Some of the frequencies obtained this way are listed in Table 1. All these modes possess the same vertical structure, but only differ in their horizontal distribution.

The horizontal structures of the 1. and 9. mode of the oscillations, which are identified by means of the low ellipses, and the corresponding horizontal velocity distributions for four successive phases ($\omega t = 0, \pi/4, \pi/2, 3\pi/4$) are displayed in Figs. 10 and 11. In Figs. 10 and 11 a each ellipse represents a trajectory of a particle, which moves periodically around the center of the respective ellipse. If a particle traverses its ellipse in the anticlockwise direction the wave motion is dominated by Kelvin-type behaviour, and ellipses are filled; if a particle traverses it in the clockwise direction this motion is primarily Poincaré-type and the ellipses are not filled. The size of the ellipses gives an indication of the excursion a particle encounters.

The motion of the 1. mode of oscillations is the rotation-modified fundamental longitudinal oscillation of the basin (Kelvin-type wave). For small lakes, this seiche period (first mode) can be calculated by a simple one-dimensional method as a function of the length of the basin, L_x, and of the phase speed c_{int} with Merian's equation

$$T_{\text{p}} = \frac{2L_x}{c_{\text{int}}}. \tag{14}$$

As the size of a lake increases or stratification decreases the effects of the rotation of the Earth become more and more important, the one-dimensional seiches with their standing waves sloshing back and forth are increasingly distorted and modified to a rotation around the basin. This is evidenced in the case treated here. The intensity of the velocity decays exponentially with the distance from shore with a strong Kelvin-type motion along the shores. The periods are, however, not significantly altered by the rotation, indeed with (14) one obtains $T_{\text{p}} = 92.6$ h compared to 103.96 h in Table 1. With an internal Rossby radius of deformation of $R_{\text{int}} = 3.8$ km in this case, which is less than a fourth of the basin width, it is clear that the effects of the rotation of the Earth must be important. The velocity field of the lowest mode is shore bound and counterclockwise around the basin (Figs. 10(b)–(f) as expected for Kelvin-type waves. The next higher (2.–6.) modes whose frequencies also lie below the inertial frequency f are likewise Kelvin-type oscillations with increasing number of amphidromic systems and are not likely to be excited by an uniform wind in the longitudinal direction of the basin. The next two modes (7. and 8., which are the first two superinertial ones) possess complex structure and are hardly excited. Mode 9., the third superinertial mode, has a simple structure (see Fig. 11); it may be interpreted as the superposition of two Poincaré waves propagating in opposite directions (see, e.g., [10]). The next, 10th and 11th modes have again intricate structures and are hardly excited.

Therefore, it seems that only the fundamental subinertial Kelvin-type oscillation (1. mode) and the 3. superinertial Poincaré-type oscillation (9. mode) can be easily excited by a spacially uniform wind. The other modes may occur under very complex wind distributions. Which of superinertial Poincaré-type oscillations actually does possess relatively simple structure depends somewhat on the influence of the Coriolis forces (on the value of the internal Rossby radius compared to the

Table 1
Eigen frequencies and periods of the fundamental oscillation (1.mode) and the first five superinertial oscillations (7., 8., 9., 10. and 11. modes) subject to the stratification (4) ($c_{\text{int}} = 39.1$ cm s^{-1}), which corresponds to a two-layer model of $h_1 = 20$ m, $h_2 = 80$ m, and $\epsilon = 9.741 \times 10^{-4}$

	Mode							
	1.	...	7.	8.	9.	10.	11.	...
Frequency [$\times 10^{-4}$ s^{-1}]	0.16787	...	1.1052	1.2421	1.3022	1.3487	1.3702	...
Period [h]	103.96	...	15.78	14.05	13.40	12.94	12.74	...

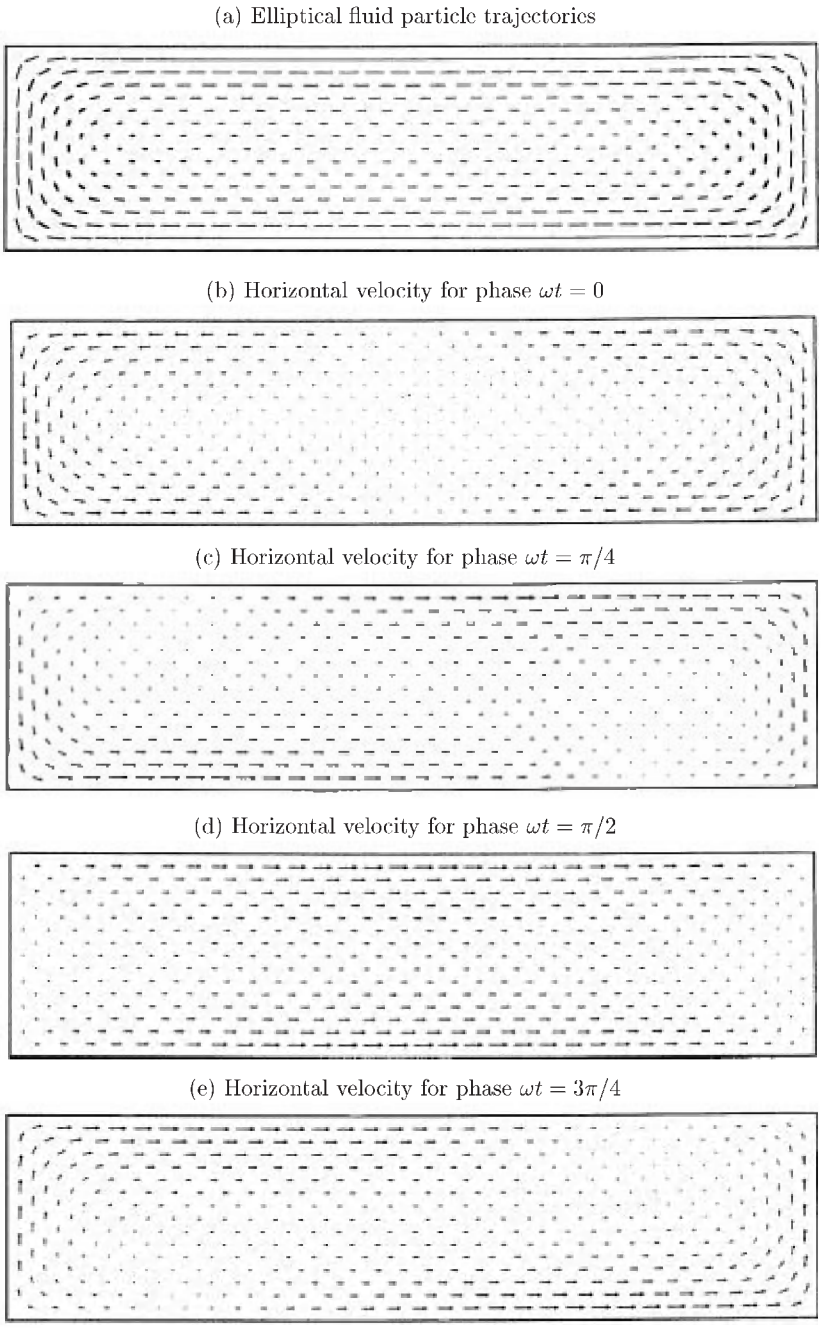

Fig. 10. Elliptical fluid particle trajectories (a) and the corresponding horizontal velocities for four successive phases (b)–(e) for the first internal oscillation mode (Kelvin-type oscillation).

width of the basin). In the calculated wind-induced circulation in Section 3 we indeed saw these two kinds of waves. Their behaviour is the same as in the eigen oscillations. Kelvin-type oscillations circulate counterclockwise around the basin and possess large amplitudes near-shore, Poincaré-type oscillations occur mainly in the center of the basin and rotate in the clockwise direction. The periods of the oscillations estimated from the wind-induced circulations and the eigen oscillations basically coincide.

5. Baroclinic oscillations in a smaller rectangular basin

In lakes, the periods of the oscillations depend on lake size, topography, and on the vertical density structure of the water body. To demonstrate the influence of basin size on the periods of baroclinic waves, the same computations as in Sections 3 and 4 are performed in this section for a smaller basin with different aspect ratio. Consider a rectangular basin of 20 km $\times$ 10 km extent and 100 m depth, initially at

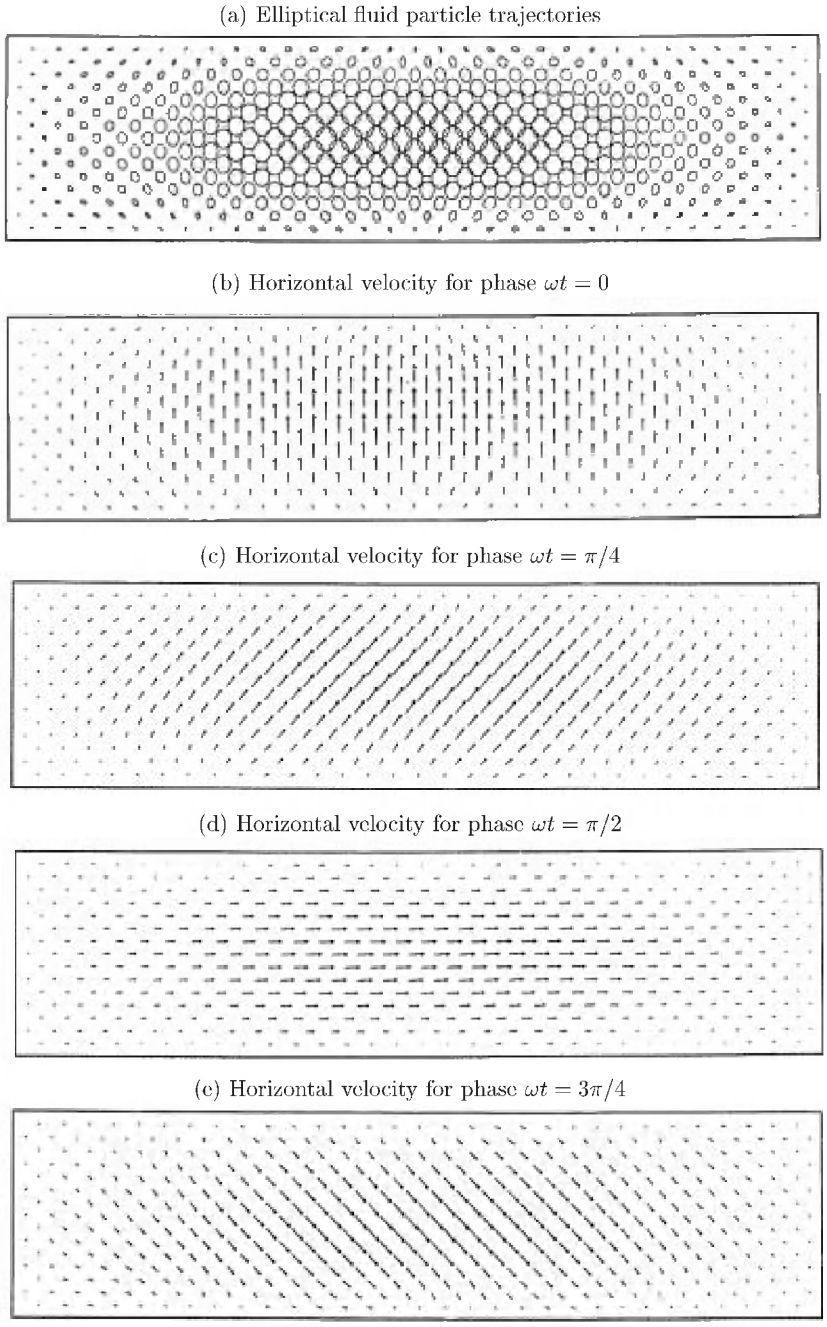

Fig. 11. Elliptical fluid particle trajectories (a) and the corresponding horizontal velocities for four successive phases (b)–(e) for the ninth internal oscillation mode (Poincaré-type oscillation).

rest, and subject to external wind-forcing in the longitudinal direction lasting two days. All other conditions and parameters are kept the same as in Section 3.

5.1. Wind-induced baroclinic response

The wind-induced circulation for this smaller basin is displayed in Fig. 12 for the longshore velocity at the mid-points of the shore around the basin. Similarly, Fig. 13 displays the two horizontal velocity components at the basin center. It is seen that two nearly periodic 'components' form the dominant signals of the computed water motion. The first (Fig. 12) possesses a period of approximately 32–33 h with amplitudes much larger near-shore than at mid-lake positions. As indicated in Fig. 12 the maxima and minima at the western/eastern near-shore mid-points are a quarter period out of phase from those at the northern/southern near-shore mid-points, facts that

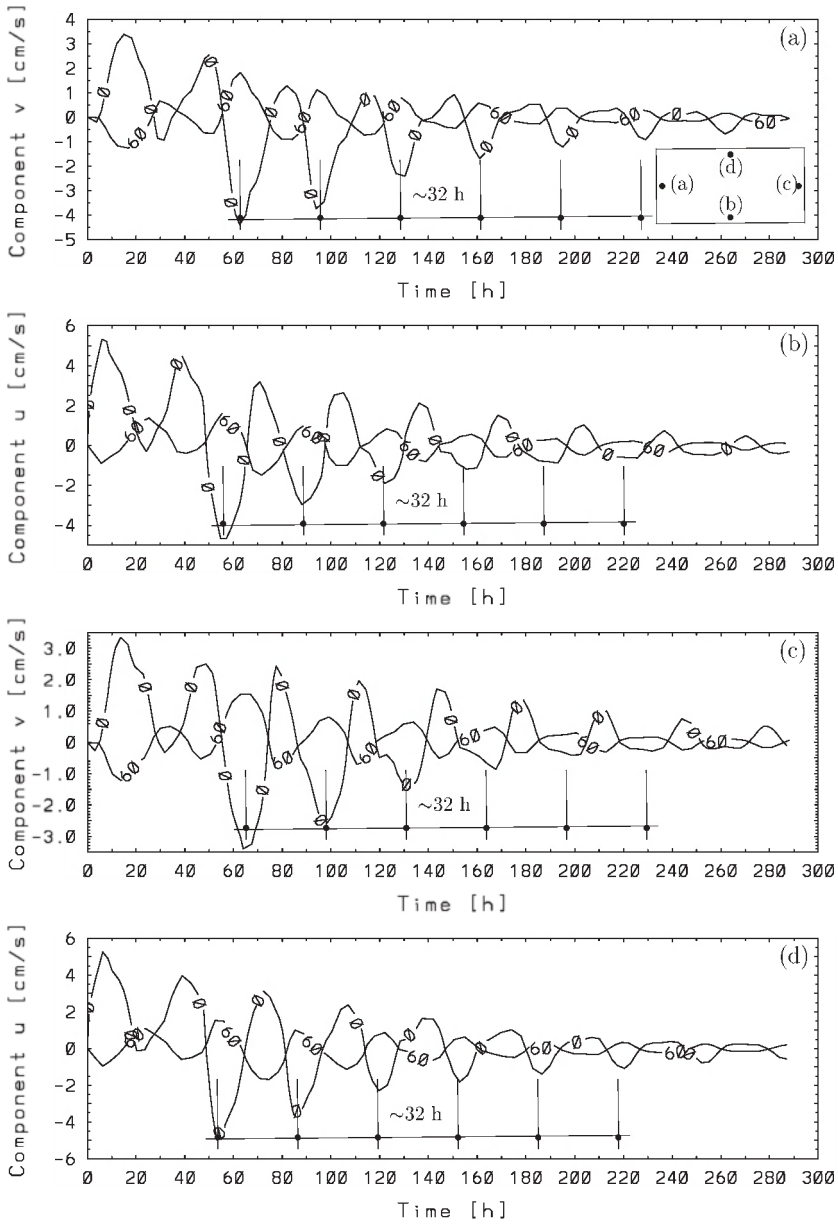

Fig. 12. Time series of the shore-parallel velocity component at the four near-shore midpoints, counterclockwise around the basin (western (a), southern (b), eastern (c) and northern shore (d)) at various depths in a stratified smaller rectangular basin of constant depth subject to a constant wind from west (in the longitudinal direction) lasting two days. The labels correspond to the depths in meters.

are reminiscent of Kelvin-type wave dynamics. The second oscillation, well visible in Fig. 13(b), has a period of approximately 10 h, is best seen in the transverse velocity components at the mid lake position, it is also seen in the mid lake longitudinal velocity components of Fig. 13(a), but they are almost completely overshadowed there by the Kelvin-type fundamental mode. Because the basin width is only about 2.5 internal Rossby radii it is also understandable why the Kelvin-type wave signal is less attenuated at the basin center than in the 65 km × 17 km basin of the last section.

5.2. Eigen oscillation

An eigenvalue problem as in Section 4 has also been solved for this smaller basin. The eigen frequencies and periods of the first five oscillations are listed in Table 2. Only the first and fifth mode, of which elliptical fluid-particle trajectories are exhibited in Fig. 14, possess structures, which are thought to be easily excited. The oscillation of the first mode propagates along the shore in the counterclockwise direction, marking Kelvin-type wave; the oscillation of the fifth mode rotates in the clockwise direction and 'lives' mainly off shore,

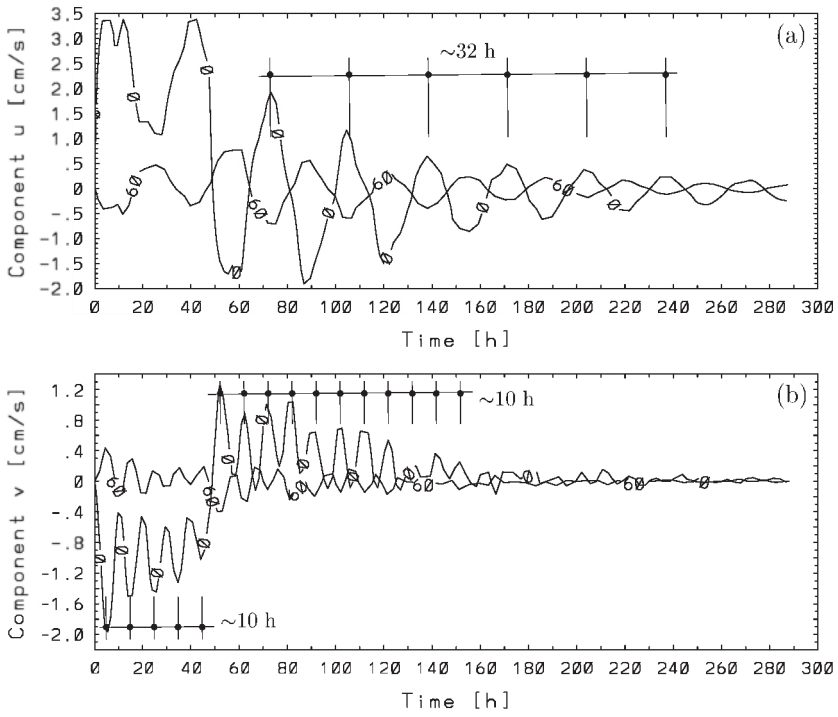

Fig. 13. Temporal evolution of the horizontal velocity components u (a) and v (b) for a midlake position in a stratified rectangular lake of constant depth (20 km × 10 km × 100 m) subject to a constant wind from west (in the across direction) lasting two days. The labels correspond to the depths in meters.

Table 2
Eigen frequencies and periods of the first five oscillations subject to the stratification (4)

	Mode					
	1.	2.	3.	4.	5.	...
Frequency [$\times 10^{-4}$ s^{-1}]	0.54773	1.0589	1.4587	1.7361	1.7676	...
Period [h]	31.9	16.5	11.5	10.05	9.9	...

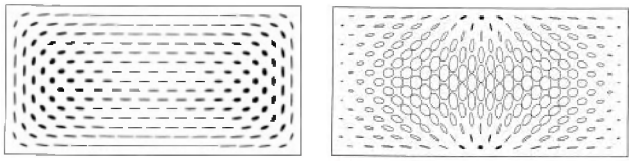

Fig. 14. Elliptical fluid particle trajectories for the 1. mode ((a), Kelvin-type oscillation) and the 5. mode ((b), Poincaré-type oscillation). Open ellipses express motions in the clockwise direction, filled ellipses mark motions in the counterclockwise direction.

indicating Poincaré-type behaviour. The corresponding periods, 31.9 and 9.9 h, respectively, are very close to those obtained from the wind-induced circulation.

6. Concluding remarks

The internal response of medium size lakes (as they exist in the Alpine regions and other mountainous areas) to wind forcings is dominated by Kelvin- and Poincaré-type wave dynamics. The circulation pattern also contains a long periodic topography induced component, but it is less significant than in the ocean and often so much damped by the bottom friction that the long periodic signals are attenuated before they have had the time to form. It follows that numerical codes must be able to reproduce the dynamics of long internal wave.

Classical codes of the shallow water equations with explicit temporal integration require large numerical diffusion to the extent that long internal waves are so quickly attenuated that the excited waves die out much faster than in reality. It is therefore important to employ semi-implicit time integration so that numerical diffusion is minimized and restricted to physically realistic values. The demonstration that our semi-implicit code SPEM enjoys these features, has been the principal goal of this paper.

We reported about the three-dimensional wind-induced baroclinic response of a rectangular basin

with constant depth. The sizes of the basins were chosen to be reminiscent of Alpine lakes. Direct response to (simple) wind forcing and the oscillating behaviour after wind secession were studied. It was demonstrated that this behaviour was well predicted, in particular, the 'life time' of the dominant Kelvin- and Poincaré-type waves were reasonably reproduced, despite the fact that the attenuation is still somewhat larger than in real lakes of comparable size.

The performance of the model can still be amended, i.e., diffusive mechanisms reduced, by using a larger number of Chebyshev polynomials, computations, however, may become unduly long. The choice of the horizontal and (more so) vertical diffusivities is very crucial, in fact the velocity field depends on the selection of the diffusivities. However, while our program allows to choose the values in the range that is thought to be physically acceptable, the vertical distribution and temporal variation can still not be chosen with sufficient assurance of physical reliability. This dictates that the Reynolds-closure conditions must be computed along with the balances of mass, momentum and energy.

A first step towards an improvement of this situation would be to add to these balance laws a closure condition of higher order, say using an algebraic formula for the Reynolds stresses or a two-parameter-closure scheme, such as the k–ε model. This has been done [3,4], however this code still faces problems of instability under very strong wind forcing.

Nevertheless, our computations over nearly 15 days indicate that non-linear wave dynamics in stratified lakes of realistic dimension can be performed, and the lake behaviour be studied. In a subsequent paper we shall do this for Lake Constance.

References

[1] Bäuerle E. Die Eigenschwingungen abgeschlossener, zweigeschichteter Wasserbecken mit variabler Topographie. Report from Institut für Meereskunde, Kiel, No. 85, 1981.

[2] Bäuerle E, Ollinger D, Ilmberger J. Some meteorological, hydrological, and hydrodynamical aspects of Upper Lake Constance. In Bäuerle E, Gaedke U, editors. Lake Constance: characterisation of an ecosystem in transition. Arch. Hydrobiol. (Special issue) 1998;53:31–83.

[3] Güting P. Dreidimensionale Berechnung windgetriebener Strömung mit einem k–ε-Modell in idealisierten Becken und dem Bodensee. Shaker 1998;343 (ISBN 3-8265-3795-5).

[4] Güting P, Hutter K. Modeling wind-induced circulation in the homogeneous Lake Constance using k–ϵ closure. Aquat Sci 1998;60:266–77.

[5] Haidvogel DB, Wilkin JL, Young R. A semi-spectral primitive equation ocean circulation model using vertical sigma and orthogonal curvilinear horizontal coordinates. J Comput Phys 1991;94:151–85.

[6] Hutter K. Fundamental equations and approximations. In: Hutter K, editor. Hydrodynamics of lakes, CISM-Lectures. Vienna: Springer; 1984a.

[7] Hutter K. Mathematische Vorhersage von barotropen und baroklinen Prozessen im Zürich- und Luganersee. Vierjahresschrift der naturforschenden Gesellschaft Zürich 1984b;129:51–92.

[8] Hutter K. Hydrodynamic modelling of lakes. Transport phenomena in the environment. Houston: Gulf Publishing; 1986. p. 897–998.

[9] Hutter K. Waves and oscillations in the ocean and in lakes. In: Hutter K, editor. Continuum mechanics in environmental sciences and geophysics. Berlin: Springer; 1993.

[10] Mortimer CH. Substantive corrections to SIL communications (IVL Mitteilun-gen) Number 6 and 20. Mitt Int Ver Theor Angew Limnol 1975;19:60–72.

[11] Peeters F. Horizontale mischung in Seen. Dissertation, ETH Zürich, 1994.

[12] Wang Y, Hutter K. A semi-implicit semi-spectral primitive equation model for lake circulation dynamics and its stability performance. J Comput Phys 1998;139:209–41.

[13] Wang Y, Hutter K. 2000a. Barotrope circulation in lakes, submitted.

[14] Wang Y, Hutter K, Bäuerle E. 2000b. Wind-induced baroclinic responses of Lake Constance. Ann Geophys, in press.